Ceramics International 50 (2024) 10974–10981

Contents lists available at ScienceDirect

Ceramics International

journal homepage: www.elsevier.com/locate/ceramint

TiB_2 effects on the $AlMgB_{14}$–TiB_2 ceramics structure and properties

Vladimir D. Valikhov [a], Ilya A. Zhukov [a], Dmitriy A. Tkachev [a], Mikhail V. Grigoriev [a], Alexey E. Matveev [a], Alex A. Volinsky [a,b,*]

[a] Department of Physics and Engineering, National Research Tomsk State University, 36 Lenin Ave., 634050, Tomsk, Russia
[b] Department of Mechanical Engineering, University of South Florida, 4202 E. Fowler Ave, ENG030, Tampa, 33620, USA

ARTICLE INFO

Handling Editor: Dr P. Vincenzini

Keywords:
$AlMgB_{14}$-TiB_2
Titanium diboride
Self-propagating high-temperature synthesis
Microhardness

ABSTRACT

This paper studied titanium diboride (TiB_2) effects on the structure and properties of $AlMgB_{14}$ ceramics. $AlMgB_{14}$–TiB_2 samples with 30 wt% and 50 wt% TiB_2 were obtained by the self-propagating high-temperature synthesis. The addition of 30 wt% TiB_2 did not significantly change the phase composition of the $AlMgB_{14}$ ceramics, which remained comparable with the initial powder mixture composition. However, increasing the TiB_2 amount to 50 wt% resulted in the $MgAl_2O_4$ spinel phase appearance. The addition of TiB_2 significantly increased the microhardness of $AlMgB_{14}$ from 7 GPa to 19.9 GPa, compared to the initial material, and also increased its flexural strength to 314 MPa.

1. Introduction

The $AlMgB_{14}$ compound was first obtained by Higashi's research group in 2000 [1]. The $AlMgB_{14}$ hardness of 32 GPa increases to 40 GPa and 46 GPa with Si or TiB_2 addition [2], pushing it towards the super-hard ceramic material class. The high hardness allows $AlMgB_{14}$ materials to become an alternative to the widely used boron nitride and diamond traditional super-hard materials. The possibility of obtaining $AlMgB_{14}$-based materials by hot pressing [3,4], self-propagating high--temperature synthesis (SHS) [5–7], and spark plasma sintering [8,9], along with their low density of 2.6 g/cm^3 [10], high 40–46 GPa hardness, and low 0.12-0.02 friction coefficient [11–13], open many possibilities in engineering applications.

$AlMgB_{14}$-based materials obtained by SHS belong to the metal-ceramics materials class. One of the main disadvantages of high-hardness ceramic materials is their high brittleness, i.e., the inability to resist dislocation motion. Metal-ceramic materials combine the properties of both metals and ceramics, achieving greater fracture toughness than traditional ceramic materials [14]. Previously, Mo and Nb were combined with ceramic materials such as Al_2O_3 and Si_3N_4 because of their high melting point, good thermal conductivity, high impact toughness, and corrosion resistance. Synthesis of ceramic composite materials with the addition of high-modulus TiB_2 particles can increase the fracture toughness of $AlMgB_{14}$-based materials. Multiple experiments have demonstrated that the TiB_2 particles not only increase the $AlMgB_{14}$ hardness [2,15], but also fracture toughness [16].

Some fundamental questions in the study of $AlMgB_{14}$-based materials include the structure and phase formation at elevated temperatures. Early research has shown that the main problem in obtaining metal-ceramic $AlMgB_{14}$-based composites at elevated temperatures is the $MgAl_2O_4$ spinel formation. Data on the phase formation in $AlMgB_{14}$ produced by hot pressing at elevated temperatures are insufficient, which makes it difficult to determine the sintering temperature modes. High-temperature resistance is one of the key parameters in the creation of products and coatings for critical applications. The aim of this work was to investigate the effects of titanium diboride on the structure, mechanical properties, and phase composition of $AlMgB_{14}$-based ceramic composites obtained by hot pressing at elevated temperatures.

2. Materials and methods

$AlMgB_{14}$ and AlB_{12} powders were synthesized by the self-propagating high-temperature synthesis (SHS). The acceptor was an $Al_{12}Mg_{17}$:B mixture with the 25:75 ratio [17]. Amorphous boron powder (B-99A, 99.9 % pure, 0.6 μm average particle size) and $Al_{12}Mg_{17}$ intermetallic alloy (98.8 % pure, 0.6 μm average particle size) were used to prepare the $Al_{12}Mg_{17}$:B mixture. The obtained powder mixture was mechanically activated in a planetary mill (Activator - 4 M, Chemical Engineering Plant Ltd., Novosibirsk, Russia) at 840 rpm for 140 min. A 40Cr13 container and SHC15SG 10 mm diameter steel balls were used. A

* Corresponding author. Department of Mechanical Engineering, University of South Florida, 4202 E. Fowler Ave. ENG030, Tampa, FL 33620, USA.
E-mail address: volinsky@usf.edu (A.A. Volinsky).

https://doi.org/10.1016/j.ceramint.2023.12.414
Received 3 October 2023; Received in revised form 29 December 2023; Accepted 31 December 2023
Available online 1 January 2024
0272-8842/Published by Elsevier Ltd.

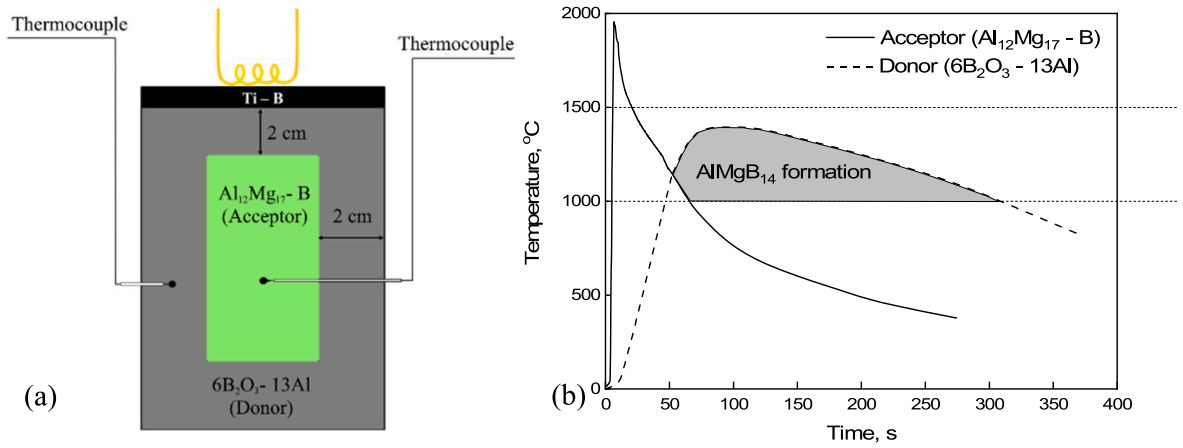

Fig. 1. (a) Schematics the $6B_2O_3$–13Al (donor)-$Al_{12}Mg_{17}$–B (acceptor) self-propagating high-temperature synthesis; (b) Thermograms of the donor ($6B_2O_3$–13Al) and acceptor ($Al_{12}Mg_{17}$–B) powder mixture fusion.

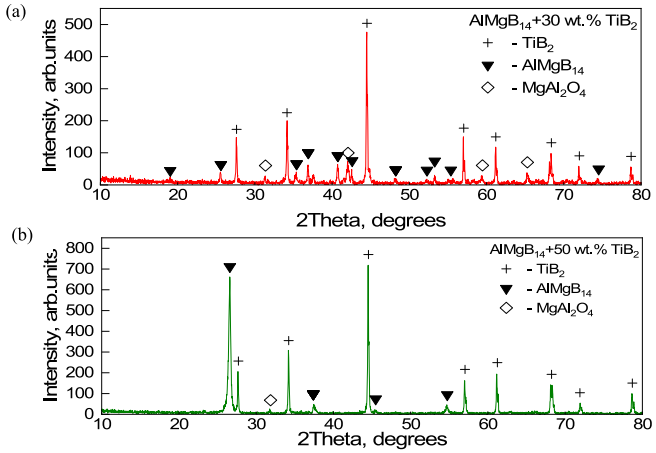

Fig. 2. X-ray diffractograms of: (a) $AlMgB_{14}$-30 wt% TiB_2; (b) $AlMgB_{14}$-50 wt% TiB_2.

mixture of 54.3 wt% B_2O_3 + 45.7 wt% Al was used as a donor according to:

$$6B_2O_3 + 13Al \rightarrow AlB_{12} + 6Al_2O_3 \quad (1)$$

B_2O_3 (Turkey, ≥99.7 % pure, ≤500 μm particle size) and Al (Sual-PM Ltd., Russia, ≥98.4 % pure, ≤100 μm particle size) powders were used to prepare the B_2O_3–Al mixture. The obtained powder mixture was mechanically activated in a planetary mill (Activator - 4M, Chemical Engineering Plant Ltd., Novosibirsk, Russia) at 840 rpm for 180 min. A 40X13 container with 10 mm diameter chrome-plated steel balls were used. The weight ratio of steel balls and powder mixture was 5:1. Air was evacuated from the steel container, forming a −0.1 MPa vacuum to suppress aluminum powder oxidation, after which it was filled with high grade argon gas. The duration of mechanical activation was 180 min, and the rotation speed of the planetary mill was 14 Hz.

A 20 g blank with a 23 mm diameter was prepared from the acceptor mixture by cold uniaxial pressing at 70 MPa. The obtained sample was placed in a cylindrical cellulose paper container. Next, the donor mixture was poured into the container until it was completely filled. The thickness of the donor mixture between the acceptor and the container

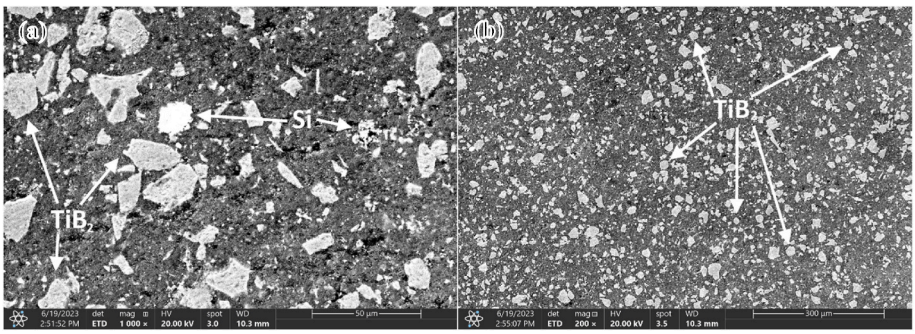

Fig. 3. SEM images of $AlMgB_{14}$–30 % TiB_2: (a) higher magnification; (b) lower magnification.

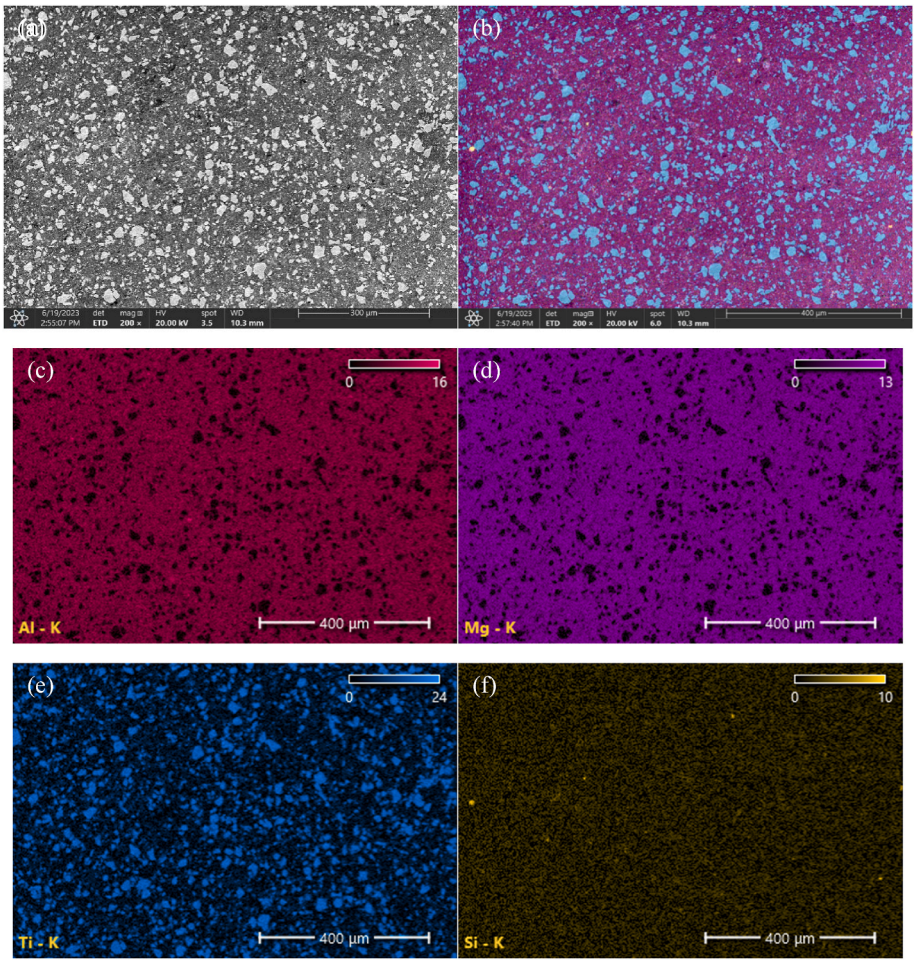

Fig. 4. Microstructure and elemental maps of $AlMgB_{14}$–30 % TiB_2: (a) SEM image; (b) all elements combined; (c) Al; (d) Mg; (e) Ti; (f) Si maps.

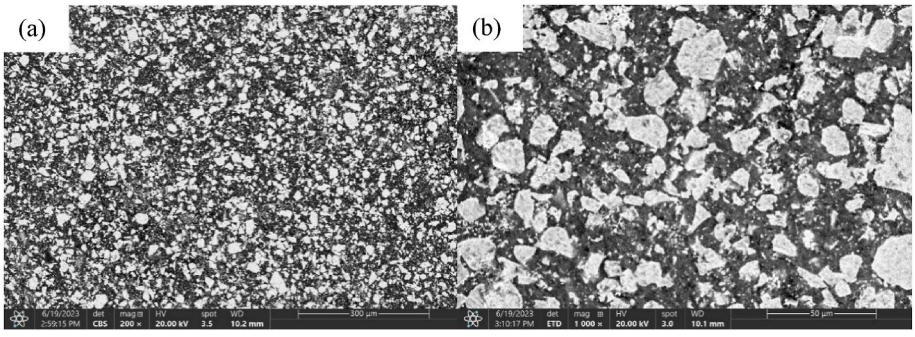

Fig. 5. SEM images of $AlMgB_{14}$–50 wt% TiB_2: (a) lower magnification; (b) higher magnification.

wall was 2 cm. The container was placed in a constant pressure reactor, which was pumped down to vacuum and filled with argon at 0.5 MPa pressure. The synthesis was initiated by a short-term heating of the upper surface of the container with a molybdenum spiral filament. A flammable layer (82.8 wt% Ti and 17.2 wt% B) was placed between the upper surface of the specimen and the filament to create a uniform heating zone. The reaction front propagation was recorded using a high-speed video camera. The synthesis temperature was monitored using tungsten-rhenium thermocouples. Schematics of the $6B_2O_3$–13Al (donor) - $Al_{12}Mg_{17}$–B (acceptor) self-propagating high-temperature synthesis is shown in Fig. 1(a) [18]. Corresponding thermograms are presented in Fig. 1(b).

$AlMgB_{14}$ and TiB_2 obtained by self-propagating high-temperature synthesis were mechanically activated separately. The obtained $AlMgB_{14}$ and TiB_2 powders were sieved to 40 μm. After sieving, $AlMgB_{14}$ and TiB_2 powders were mechanically activated in a planetary mill at 70:30 and 50:50 wt% ratios, respectively. The obtained mechanical mixtures of $AlMgB_{14}$+30 wt% TiB_2 and $AlMgB_{14}$+50 wt% TiB_2 were compacted by hot pressing at 35 MPa pressure and 1500 °C in argon atmosphere. This temperature was selected based on a previous study [19], which indicated that the 1500 °C is optimal temperature for the $AlMgB_{14}$-based materials synthesis.

The structure and elemental composition of the $AlMgB_{14}$ materials with 30 wt% and 50 wt% titanium diboride obtained by 35 MPa hot pressing in argon at 1500 °C were investigated using scanning electron microscopy (SEM, Axia ChemiSEM Thermo Scientific, FEI, USA). The

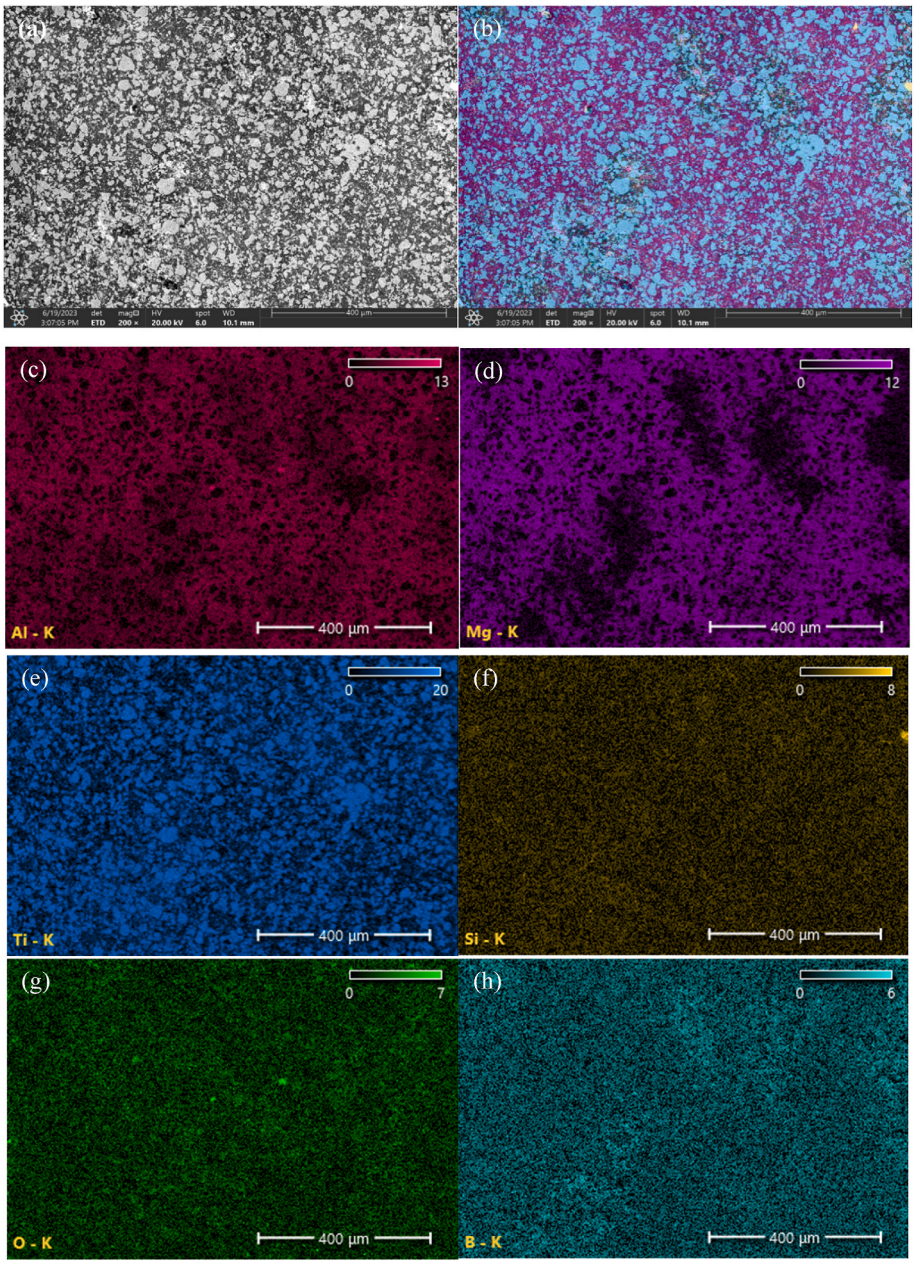

Fig. 6. Microstructure and elemental maps of $AlMgB_{14}$-50 wt% TiB_2: (a) SEM image; (b) all elements combined; (c) Al; (d) Mg; (e) Ti; (f) Si; (g) O; (h) B maps.

Table 1
The microhardness of $AlMgB_{14}$-30 wt% TiB_2 and $AlMgB_{14}$-50 wt% TiB_2 composites.

Sample	Microhardness, kgf/mm^2	Microhardness, GPa
$AlMgB_{14}$ (1500 °C) [16]	718 ± 70	7 ± 0.68
$AlMgB_{14}$-30 wt% TiB_2	1081 ± 110	10.6 ± 1.08
$AlMgB_{14}$-50 wt% TiB_2	2035 ± 150	19.9 ± 1.47

density of the hot-pressed samples was calculated using the Archimedes method. X-ray phase analysis of samples was carried out using a Shimadzu XRD-7000 X-ray diffractometer with the following scanning parameters: 20–90° 2θ diffraction angle range with 0.04° scanning step, and 3 s exposure at each point. Three-point bending tests were performed using an Instron 3369 universal testing machine with a moving crosshead speed of 0.2 mm/min [20]. Microhardness was determined using the Vickers method [21] with a 300 g load and 20 s hold time (Metolab 503, Moscow, Russia).

3. Results and discussion

3.1. X-ray diffraction analysis

The X-ray phase analysis results in Fig. 2(a) showed that in addition to the original $AlMgB_{14}$ and TiB_2 phases, the samples containing 30 wt%

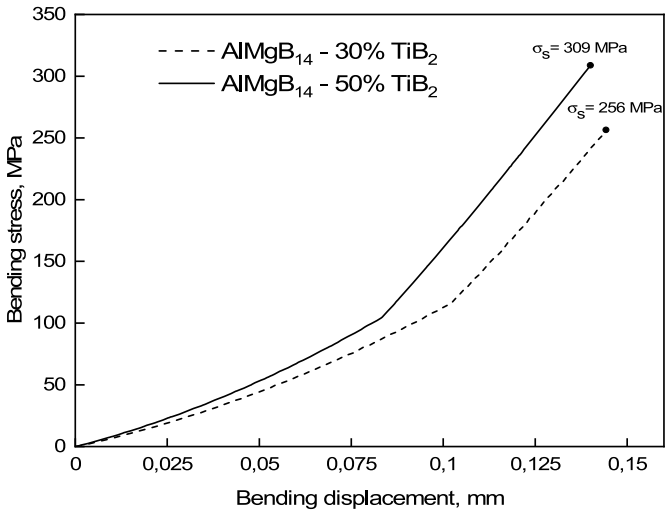

Fig. 7. Stress-displacement curves of $AlMgB_{14}$–TiB_2 under three-point bending.

TiB_2 also had spinel $MgAl_2O_3$ phase. However, in the sample containing 50 wt% TiB_2, the presence of four phases is observed in Fig. 2(b): TiB_2, $MgAlB_{14}$, $MgAl_2O_4$, and $MgAlB_4$ with a concentration of 64 wt%, 5 wt%, 5 wt% and 26 wt%, respectively, which does not correspond to the composition of the original material and materials containing 30 wt% TiB_2.

The phase analysis results in Fig. 2(a) show that the $AlMgB_{14}$-30 wt% TiB_2 sample contains 68 wt% $AlMgB_{14}$ phase with a = 5.8532 Å, b = 10.3066 Å, c = 8.1107 Å lattice parameters and 72 nm average size of crystallites, while the remaining 23 wt% TiB_2 phase has the a = 3.0285 Å and c = 3.2286 Å lattice parameters, and 91 nm average size of crystallites. A spinel $MgAl_2O_4$ phase was also found with a content of 9 wt% and a = 8.083 Å.

In Fig. 2(b) the $AlMgB_{14}$-50 wt% TiB_2 metal-ceramic composite phase composition is represented by the 64 wt% TiB_2 phase with a = 3.0309 Å and c = 3.2310 Å lattice parameters, and 93 nm average size of crystallites, calculated from the Scherrer's formula. The $AlMgB_{14}$ phase in the 31 wt% amount has a = 5.8449 Å, b = 10.3183, c = 8.1294 Å lattice parameters and 60 nm average size of crystallites. This sample also contains 5 wt% $MgAl_2O_4$ spinel phase with a = 7.8786 Å lattice parameter and 10 nm average crystallites' size.

3.2. Structure of $AlMgB_{14}$-30 wt% TiB_2

Characterization of the $AlMgB_{14}$-based ceramic composites structure and phase composition demonstrated that the material obtained by 1500 °C hot pressing had the highest density [19]. Similar temperature and pressure were used for the $AlMgB_{14}$ synthesis with 30 wt% and 50 wt% TiB_2 in this paper. The obtained material with 30 wt% TiB_2 has 2.5 g/cm^3 density and 22 % porosity.

SEM images are presented in Fig. 3, where TiB_2 particles have an irregular shape. Most of the larger particles have 40–45 μm average size. Particles with an 5–8 μm average size are also present, suggesting a bimodal size distribution of the TiB_2 particles.

Energy-dispersive X-ray spectroscopy (EDS) mapping of elements in Fig. 4 shows that the composite matrix consists of Al, Mg and B. B mapping was not performed because it is a part of both matrix and TiB_2 particles and is present in the combined map in Fig. 4(b) as a solid background. Titanium diboride particles are uniformly distributed in the $AlMgB_{14}$ matrix. The average particle size is 40 μm, which corresponds to the sieving cell size used in the preparation of powders for hot pressing. The maps also show particles with Si, possibly due to inclusions of silicon carbide, which is the abrasive material of the sandpaper.

3.3. Structure of $AlMgB_{14}$-50 wt% TiB_2

Fig. 5 shows the structure of $AlMgB_{14}$-based ceramics with 50 wt% TiB_2. The titanium diboride particles are uniformly distributed throughout the matrix and do not form clusters or agglomerates. Similar to the $AlMgB_{14}$-30 wt% TiB_2 sample, the diboride particles distribution is bimodal with the 40–45 μm larger particles and 5–8 μm smaller particles. The density of the sample measured by hydrostatic weighing is 3.19 g/cm^3. The porosity of the obtained material is 11 %, which is 2 times less than the porosity of samples containing 30 wt% TiB_2.

Elemental mapping reveals that some areas show an increase in boron intensity, a strong decrease in magnesium intensity, and a weak decrease in aluminum intensity. Presumably, this may be a consequence of local overheating of material sections due to clustering of TiB_2 particles.

In Fig. 6(c) and (g) one can see bright formations that may be aluminum and oxygen compound, such as Al_2O_3. Silicon is also present. The presence of these inclusions can be explained by the process of sample surface preparation prior to microscopic examination. The surface of the samples was ground with SiC-based abrasive paper and polished with Al_2O_3-based slurry.

3.4. Mechanical properties

The microhardness of $AlMgB_{14}$-30 wt% TiB_2 and $AlMgB_{14}$-50 wt% TiB_2 composites is listed in Table 1. The microhardness of the $AlMgB_{14}$-30 wt% TiB_2 sample is 10.6 GPa, which is 3 GPa higher than the microhardness of the $AlMgB_{14}$ obtained in Ref. [16]. Increasing the TiB_2 content to 50 wt% leads to an increased microhardness of 19.9 GPa. Microhardness measurements show that the difference between pure $AlMgB_{14}$ and $AlMgB_{14}$- 50 wt% TiB_2 is 150 %, in other words, the addition of 50 wt% titanium diboride increases the microhardness of $AlMgB_{14}$-based materials by 2.5 times.

Three-point bending results are presented in Fig. 7. The stress-

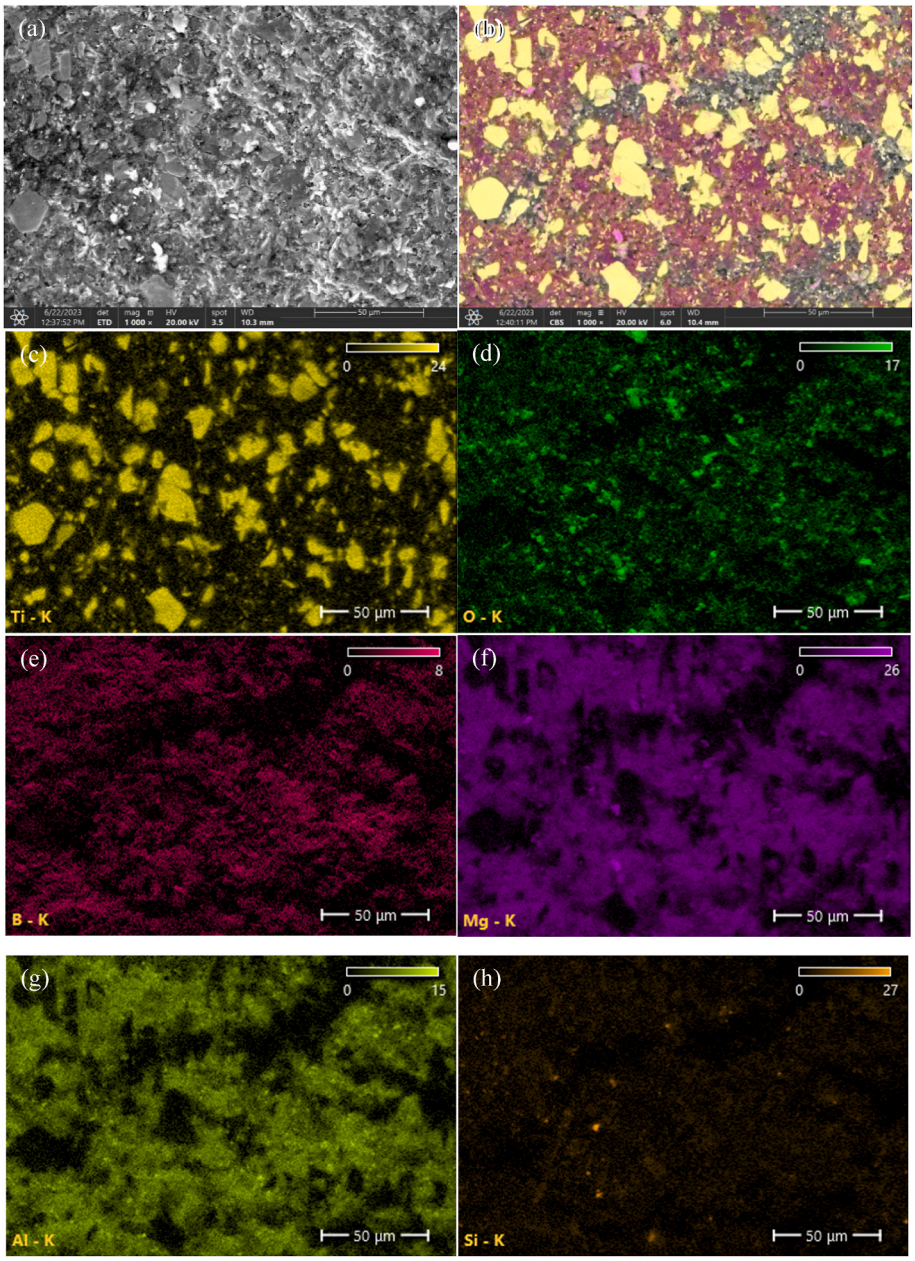

Fig. 8. EDS fracture surface analysis and elemental maps of $AlMgB_{14}$-30 wt% TiB_2: (a) SEM image of the fracture surface; (b) all elements combined; (c) Ti; (d) O; (e) B; (f) Mg; (g) Al; (h) Si maps.

displacement diagrams show that the flexural strength of the $AlMgB_{14}$ specimen with 50 wt% TiB_2 is 309 MPa, while the flexural strength of the $AlMgB_{14}$-30 wt% TiB_2 specimen is 256 MPa, which is 53 MPa lower.

The bending tests data of ceramic composite materials based on $AlMgB_{14}$ obtained at different hot-pressing temperatures are presented in Ref. [19]. The maximum flexural strength of 314 MPa was obtained for the specimen hot pressed at 1500 °C. This value exceeds the bending strength of the $AlMgB_{14}$-50 wt% TiB_2 sample by 5 MPa, which is within the measurement error. At the same time, the maximum bending displacement for samples with titanium diboride is 0.14 mm and 0.15 mm, which is 40–50 % higher than the 0.1 mm for the samples without TiB_2. The 256 MPa flexural strength of the $AlMgB_{14}$-50 wt% TiB_2 sample compared to the 309 MPa of the $AlMgB_{14}$-30 wt% TiB_2 sample can be attributed to the higher 3.19 g/cm^3 density of the 50 wt% TiB_2 sample (vs. 2.5 g/cm^3) and lower 11 % porosity (vs. 22 %). The introduction of titanium diboride contributes to an increase in the bending displacement, which can be attributed to an increased fracture toughness [16].

3.5. Fracture analysis

The fractographic results showed that brittle fracture was predominant in the fracture of $AlMgB_{14}$ with the addition of 30 wt% in Fig. 8 and 50 wt% TiB_2 in Fig. 9. The fracture surface in Fig. 8(a) shows that the TiB_2 particles fractured by brittle fracture mechanism. The fracture of the particles shows traces with radial bands, characteristic of brittle fracture without shear stresses in Fig. 9(a).

The phase composition dependence of the $AlMgB_{14}$–TiB_2 metal-ceramic composites on the introduced TiB_2 mass is almost linear in

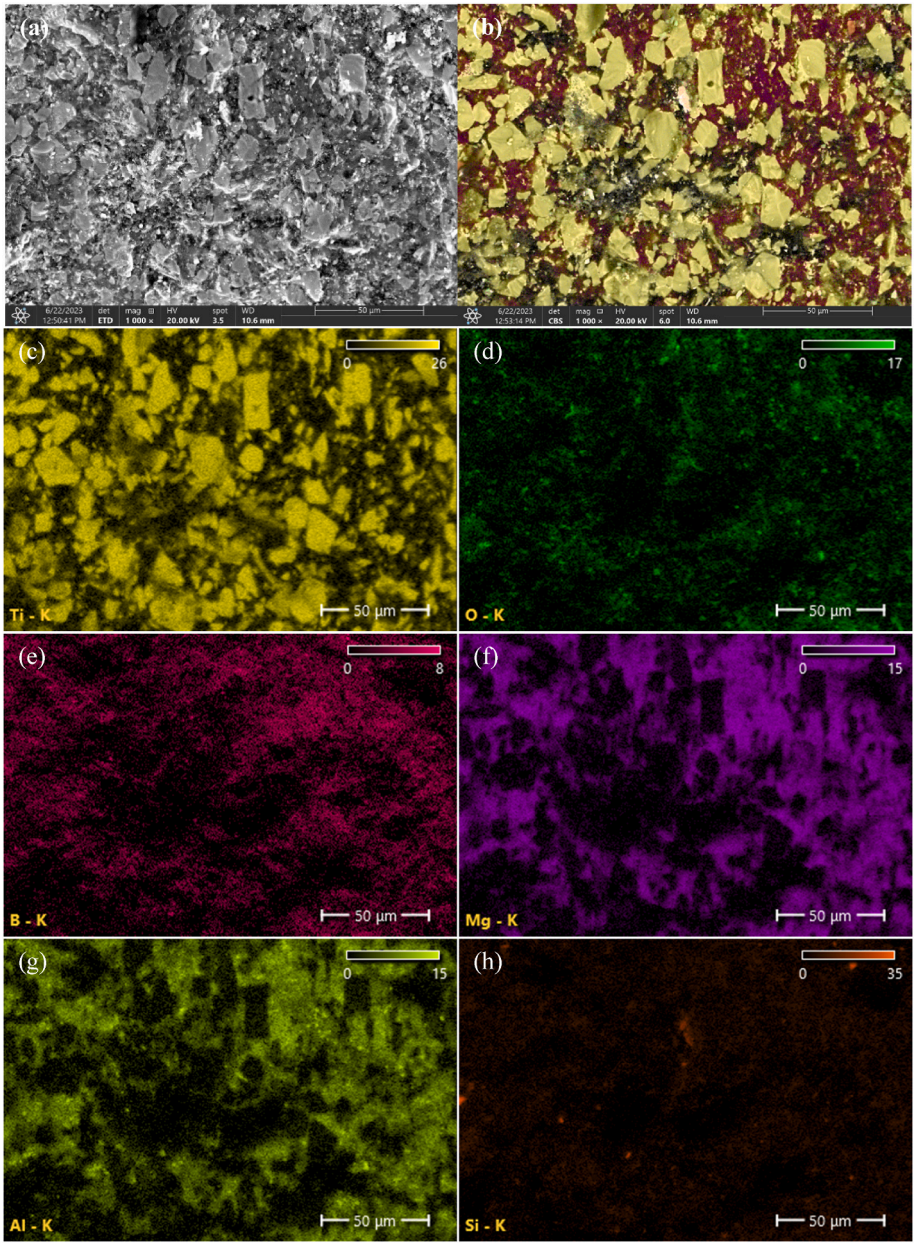

Fig. 9. EDS fracture surface analysis of $AlMgB_{14}$-50 wt% TiB_2: (a) SEM image of the fracture surface; (b) all elements combined; (c) Ti; (d) O; (e) B; (f) Mg; (g) Al; (h) Si maps.

Fig. 10. This means that the introduced TiB_2 is stable during 1500 °C hot-pressing, which is also confirmed by EDS analysis. The effect of TiB_2 mass content on the microhardness of $AlMgB_{14}$ has a nonlinear character, and approaches exponential dependence in Fig. 10. Increasing the amount of titanium diboride particles leads to higher Vickers microhardness.

4. Conclusions

1. The introduction of TiB_2 in the 30 wt% and 50 wt% amounts allows to reach the flexural strength of 256 MPa and 309 MPa, respectively. The corresponding bending displacements are 0.14 mm and 0.15 mm, respectively. Compared to Ref. [19], were $AlMgB_{14}$-based materials were prepared using a similar technology, the magnitude of bending displacement increased by 40–50 %. The microhardness of the ceramic composites is 10.6 GPa and 19.9 GPa for 30 wt% and 50 wt% TiB_2, respectively.
2. The distribution of titanium diboride over the ceramic matrix volume is uniform. TiB_2 particles have a bimodal size distribution of 40–45 μm and 5–8 μm. The main compound Al, Mg, B, and Ti elements are evenly distributed in the $AlMgB_{14}$-30 wt% TiB_2 structure, along with separate Al_2O_3 and SiC particles.
3. The phase composition of the $AlMgB_{14}$-30 wt% TiB_2 metal-ceramic composite corresponds to the initial powder mixture composition and is represented by the $AlMgB_{14}$ and TiB_2 phases in the 66 wt% and 34 wt% amounts. In addition to the initial powder mixture components, the $AlMgB_{14}$-50 wt% TiB_2 composites contains 11 wt% of spinel $MgAl_2O_4$.

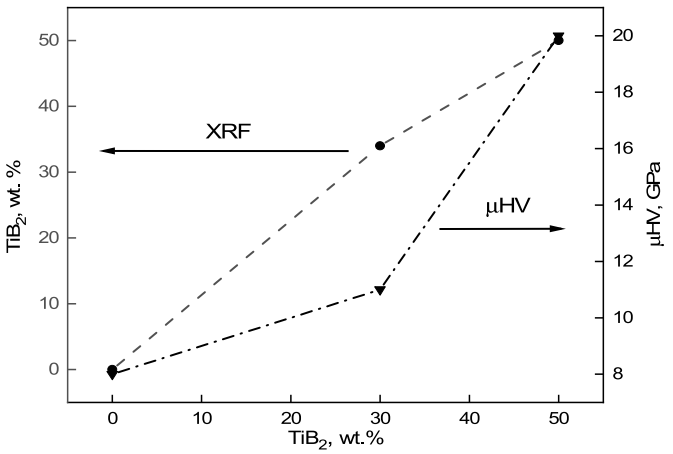

Fig. 10. Microhardness and phase composition of TiB_2.

4. The study of the fracture surface of the samples indicates the brittle nature of fracture of the metal-ceramic composite based on $AlMgB_{14}$ with 30 wt% and 50 wt% TiB_2. Titanium diboride particles undergo brittle fracture with a ductile component. This is evidenced by the radial lines remaining on the fractured TiB_2 particles.

Declaration of competing interest

The authors declare that they have no known competing financial interests or personal relationships that could have appeared to influence the work reported in this paper.

Acknowledgements

The study was supported by the Russian Science Foundation Grant No. 19-79-10042. This research was carried out using the equipment of Tomsk Regional Core Shared Research Facilities Center of National Research Tomsk State University. The Center was supported by the Ministry of Science and Higher Education of the Russian Federation Grant No. 075-15-2021-693 (No. 13. RFC.21.0012).

References

[1] I. Higashi, M. Kobayashi, S. Okada, K. Hamano, T. Lundström, Boron-rich crystals in Al-M-B (M = Li, Be, Mg) systems grown from high-temperature aluminum solutions, J. Cryst. Growth 128 (1993) 1113–1119, https://doi.org/10.1016/S0022-0248(07)80108-4.

[2] B.A. Cook, J.L. Harringa, T.L. Lewis, A.M. Russell, A new class of ultra-hard materials based on AlMgB14, Scripta Mater. 42 (2000) 597–602, https://doi.org/10.1016/S1359-6462(99)00400-5.

[3] J. Jiang, J. Xie, H. Zhong, F. Dong, N. Liu, W. Tang, H. Zhu, J. Jiang, Synthesis and mechanical properties of $AlMgB_{14}$–Al composite, J. Alloys Compd. 818 (2020) 152910, https://doi.org/10.1016/j.jallcom.2019.152910.

[4] Y. Zhou, F. Zhang, L. Pengcheng, K. Bai, W. Shanghua, S. Luo, Synthesis and characterization of AlMgB14 hot pressed under different environments, Sci. Sint. 49 (2017) 311–317, https://doi.org/10.2298/SOS1703311Y.

[5] P. Yu Nikitin, I.A. Zhukov, A.E. Matveev, S.D. Sokolov, M.S. Boldin, A. B. Vorozhtsov, $AlMgB_{14}$–TiB_2 composite materials obtained by self-propagating high-temperature synthesis and spark plasma sintering, Ceram. Int. 46 (2020) 22733–22737, https://doi.org/10.1016/j.ceramint.2020.06.039.

[6] P.Y. Nikitin, A.E. Matveev, I.A. Zhukov, Energy-effective $AlMgB_{14}$ production by self-propagating high-temperature synthesis (SHS) using the chemical furnace as a source of heat energy, Ceram. Int. 47 (2021) 21698–21704, https://doi.org/10.1016/j.ceramint.2020.06.039.

[7] P. Yu Nikitin, Yu A. Abzaev, A.E. Matveev, I.A. Zhukov, O.G. Volokitin, Phase content, structural and thermodynamic properties of $AlMgB_{14}$, obtained by SHS using the chemical furnace, AIP Conf. Proc. 2509 (2022) 020142, https://doi.org/10.1063/5.0084234.

[8] P. Nikitin, I. Zhukov, A. Matveev, S. Sokolov, M. Grigoriev, A. Vorozhtsov, On the structure and properties of $AlMgB_{14}$-TiB_2 composites obtained from SHS powders by spark plasma sintering, Mater 14 (2021) 5521, https://doi.org/10.3390/ma14195521.

[9] Y.M. Zhou, T. Zhang, K. Xu, F.L. Zhang, K. Bai, H.P. Huang, S.H. Wu, S.M. Luo, Effect of Y_2O_3 addition on microstructure and mechanical properties of spark plasma sintered $AlMgB_{14}$ and $AlMgB_{14}$-TiB_2, Ceram. Int. 44 (2018) 8591–8598, https://doi.org/10.1016/j.ceramint.2018.02.073.

[10] V.I. Matkovich, J. Economy, Structure of MgAlB14 and a brief critique of structural relationships in higher borides, Acta Crystallogr. B 26 (1970) 616–621, https://doi.org/10.1107/S0567740870002868.

[11] C. Higdon, B. Cook, J. Harringa, A. Russell, J. Goldsmith, J. Qu, P. Blau, Friction and wear mechanisms in $AlMgB_{14}$-TiB_2 nanocoatings, Wear 271 (2011) 2111–2115, https://doi.org/10.1016/j.wear.2010.11.044.

[12] B.A. Cook, J.L. Harringa, J. Anderegg, A.M. Russell, J. Qu, P.J. Blau, C. Higdon, A. A. Elmoursi, Analysis of wear mechanisms in low-friction $AlMgB_{14}$–TiB_2 coatings, Surf. Coat. Technol. 205 (2010) 2296–2301, https://doi.org/10.1016/j.surfcoat.2010.09.007.

[13] J. Qu, P.J. Blau, D. Zhu, B.A. Cook, A.A. Elmoursi, Tribological Characteristics of AlMgB14 and Nanocomposite $AlMgB_{14}$-TiB_2 Superhard Coatings. IJTC2008, vol. 43369, 2008, pp. 757–759, https://doi.org/10.1115/IJTC2008-71176.

[14] L. Yajing, Z. Zengda, H. Xian, A study of brazing the interphase of WC–TiC–Co hardmetals, Int. J. Refract. Met. Hard Mater. 20 (2002) 169–173, https://doi.org/10.1016/S0263-4368(01)00061-0.

[15] Yu M. Zhou, F.L. Zhang, P.C. Li, K. Bai, S.H. Wu, A study on ultra-hard $AlMgB_{14}$ modified by TiB_2 and Ni_3Al, Mater. Sci. Forum 848 (2016) 607–612. https://doi.org/10.4028/www.scientific.net/MSF.848.607.

[16] A. Ahmed, S. Bahadur, B.A. Cook, J. Peters, Mechanical properties and scratch test studies of new ultra-hard $AlMgB_{14}$ modified by TiB_2, Tribol. Int. 39 (2006) 129–137, https://doi.org/10.1016/j.triboint.2005.04.012.

[17] I.A. Zhukov, P.Y. Nikitin, A.B. Vorozhtsov, S.N. Perevislov, S.D. Sokolov, M. H. Ziatdinov, The use of intermetallic Al_xMg_y powder to obtain $AlMgB_{14}$-based materials, Mater. Today Commun. 22 (2020) 100848, https://doi.org/10.1016/j.mtcomm.2019.100848.

[18] A.E. Matveev, I.A. Belchikov, I.A. Zhukov, Mechanical activation time of $6B_2O_3$–13Al powder mixture vs. structure and phase composition of SHS products, Ceram. Int. 49 (2023) 16564–16577, https://doi.org/10.1016/j.ceramint.2023.02.014.

[19] D. Tkachev, P. Nikitin, I. Zhukov, A. Vorozhtsov, E. Marchenko, Y. Verkhoshanskiy, I. Belchikov, Structure and flexural strength of the hot-pressed $AlMgB_{14}$ ceramic, Phys. Scripta 98 (2023) 025703, https://doi.org/10.1088/1402-4896/acaeea.

[20] ISO 17138, Fine Ceramics (Advanced Ceramics, Advanced Technical Ceramics)—Mechanical Properties of Ceramic Composites at Room Temperature—Determination of Flexural Strength, 2014.

[21] C28 Committee, Test Method for Vickers Indentation Hardness of Advanced Ceramics, ASTM International), West Conshohocken, PA, 2019.